ARTICLES
https://doi.org/10.1038/s41561-020-0609-y

nature geoscience

Check for updates

Preferential localized thinning of lithospheric mantle in the melt-poor Malawi Rift

Emily Hopper[1]✉, James B. Gaherty[2], Donna J. Shillington[2], Natalie J. Accardo[1], Andrew A. Nyblade[3], Benjamin K. Holtzman[1], Christopher Havlin[1], Christopher A. Scholz[4], Patrick R. N. Chindandali[5], Richard W. Ferdinand[6], Gabriel D. Mulibo[6] and Gabriel Mbogoni[7]

The forces required to initiate rifting in cratonic plates far exceed the available tectonic forces. High temperatures and resultant melts can weaken the lithosphere, but these factors do not readily explain the extension of old and strong lithosphere in magma-poor rifts, such as the Malawi Rift. Here, new seismic converted-wave imaging shows that even in this magma-poor rift, upper-crustal rift basins are associated with localized preferential thinning of the lithospheric mantle. We calculated the beta factor, the ratio between current and prerift thickness, beneath the rift axis and found crustal beta of 1.7 ± 0.3 and lithospheric-mantle beta of 3.8 ± 1.7. Purely mechanical stretching cannot explain the preferential lithospheric mantle thinning—instead, thinning of the rheological lithosphere was probably augmented by thermochemical rejuvenation and erosion. Although local surface-wave-derived shear-wave velocities preclude a substantially elevated temperature and partial melt today, fusible materials preserved in the lower lithosphere that underlie the Ubendian Belt and its bounding subduction-related sutures in which the Malawi Rift nucleated may have provided an early supply of melt that enabled localized lithospheric alteration and/or removal. A plume-related or other asthenospheric perturbation would preferentially melt the more fusible lithospheric materials and the rising melts would heat and weaken progressively shallower parts of the lithosphere, which spatially localizes weakening (hence the lithospheric-mantle thinning) and enables the onset of rifting.

Continental rifting is the first step in continental breakup and the formation of new ocean basins. Rifted margins that line these basins demonstrate that breakup occurs under a range of conditions with varying amounts of magmatism. Yet how does intact continental lithosphere rift if lithospheric yield strengths may be an order of magnitude higher than the available tectonic forces[1,2]? Magmatism may weaken the lithosphere by increasing buoyancy, heat and metasomatism, and thereby reduce the required forces[2]. Pre-existing structures are suggested to control rift location[3], although substantial localized weakening would still be needed to account for the force discrepancy. Alternatively, large-scale conductive warming, weakening and perhaps removal of the lithosphere would reduce the required forcing without melt[4,5]. Each of these end-member mechanisms produce different responses in the crust, lithospheric mantle and asthenosphere. Therefore, to test these models, we must image each of these components.

The 3,000-km-long seismically and volcanically active East African Rift System (Fig. 1a) is the classic example of an active continental rift associated with a plume[6,7]. Voluminous magmatism is associated with much of the East African Rift, particularly the Eastern Branch[8,9]. In contrast, the Western Branch magmatism is limited to isolated volcanic centres[7], with a lava geochemistry that indicates lithospheric metasomatism and a plume influence in at least the youngest lavas[6,7]. The lithosphere is generally old[10] and strong[11,12], with a seismically fast[13–15], resistive[16] lithosphere up to 200 km in thickness imaged just off axis.

Most observations of localized lithospheric thinning in active continental rifts come from highly magmatic rifts, such as the Main Ethiopian Rift[8], in which voluminous magmatism and/or high mantle temperatures provide a clear explanation for lithospheric-mantle removal and/or modification over an area up to a width of 500 km (refs [8,17]). However, constraints on lithospheric thinning from the magma-poor Western Rift are sparse.

Here we focus on the Malawi Rift in the southern Western Branch (Fig. 1b), an early-stage rift in a strong continental lithosphere with limited volcanism and a typical upper-crustal morphology—seismically active, deep asymmetric half-grabens consistent with a strong lithosphere. Crustal extension initiated at least 8.6 million years ago (Ma) (ref. [18]), perhaps 25 Ma (ref. [19]), albeit at slow rates (1–4 mm yr^{-1})[20] and with ≤7 km (ref. [21]) cumulative crustal extension. The recent SEGMeNT (Study of Extension and Magmatism in Malawi and Tanzania) experiment[22] in and around Lake Malawi (Nyasa) allows unprecedented resolution of the crust and upper mantle here.

We present new common-conversion-point stacked S-to-P (Sp) and P-to-S (Ps) converted-wave imaging of the lithosphere from events recorded on 74 stations, which include 59 SEGMeNT stations, 5 of which were deployed on the floor of Lake Malawi (Fig. 1b). In our images, positive velocity gradients (PVGs) with increasing depth are red and negative velocity gradients (NVGs) are blue (Fig. 2). We discuss the crust–mantle boundary (Moho), a PVG, and the lithosphere–asthenosphere boundary (LAB), an NVG. The LAB is a rheological boundary that separates conductive lithosphere from convective asthenosphere, associated with a seismic velocity drop[23]. In our study area, the rheological LAB may be a boundary between an unmodified shallow lithosphere with high seismic velocities and a seismically slower, pervasively altered, previously lithospheric mantle that is rheologically now asthenosphere (as suggested for the Albert–Edward Rift[24]), rather than upwelled asthenosphere.

[1]Lamont-Doherty Earth Observatory, Palisades, NY, USA. [2]Northern Arizona University, Flagstaff, AZ, USA. [3]Pennsylvania State University, State College, PA, USA. [4]Syracuse University, Syracuse, NY, USA. [5]Geological Survey of Malawi, Zomba, Malawi. [6]University of Dar es Salaam, Dar es Salaam, Tanzania. [7]Geological Survey of Tanzania, Dodoma, Tanzania. ✉e-mail: ehopper@ldeo.columbia.edu

Content courtesy of Springer Nature, terms of use apply. Rights reserved

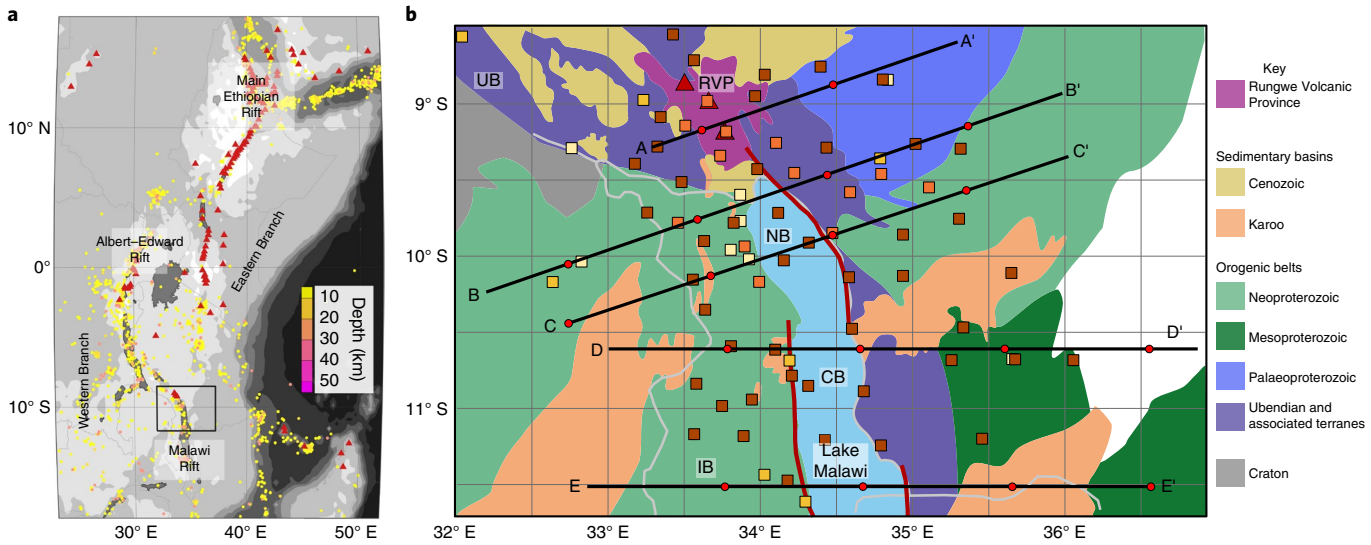


Fig. 1 | Maps of the study region. a, Overview map of the East African Rift System. Circles, earthquakes, coloured by depth; triangles, Holocene volcanism; greyscale shading, topography and bathymetry; black box locates panel **b**. **b**, Geological summary map[14]. Red lines show major Cenozoic normal faults around Lake Malawi[21]. RVP, Rungwe Volcanic Province; UB, Ubendian Belt; IB, Irumide Belt; NB, North Basin; CB, Central Basin. Orange squares, SEGMeNT seismic stations (dark, used for both Sp and Ps imaging; light, used for Ps only); yellow squares, SAFARI, Africa Array and other existing seismic stations (gold, Sp and Ps; pale yellow, Ps). Black lines show cross-section locations (Fig. 2).

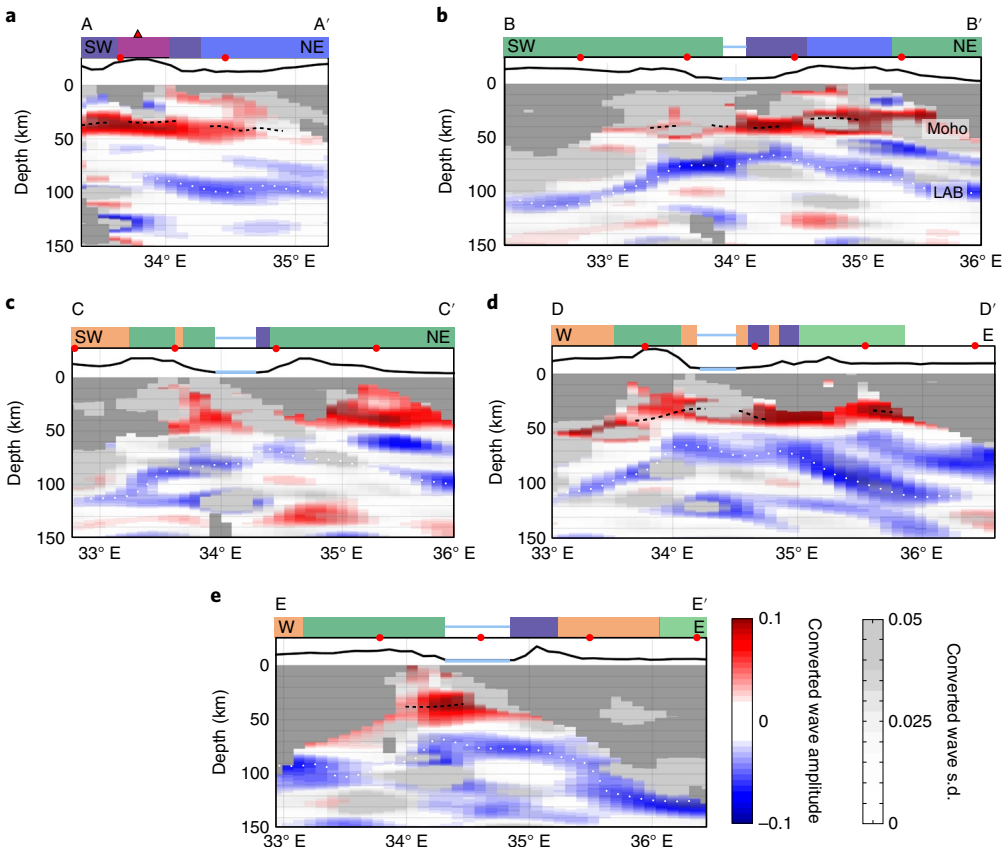


Fig. 2 | Lithospheric structure beneath Lake Malawi. a–**e**, Cross-sections A–A′ (**a**), B–B′ (**b**), C–C′ (**c**), D–D′ (**d**) and E–E′ (**e**) (Fig. 1b) are through the mean bootstrapped 4–100 s Sp common-conversion-point stack, masked by standard deviation (s.d.) between bootstraps (right-hand shaded bar) or fewer than ten contributing waveforms (dark grey), with no vertical exaggeration. Dotted white line, LAB, picked from this Sp stack; dashed black line, Moho, picked from the higher-resolution Ps stack (Extended Data Fig. 1). If no clear Moho was imaged by Ps, this line is omitted, for example C–C′. Red circles correspond to those on the location map (Fig. 1b). Shaded boxes correspond to terranes (Fig. 1b). The solid black lines show the topography with a 10× vertical exaggeration, and the blue lines show Lake Malawi.

Content courtesy of Springer Nature, terms of use apply. Rights reserved

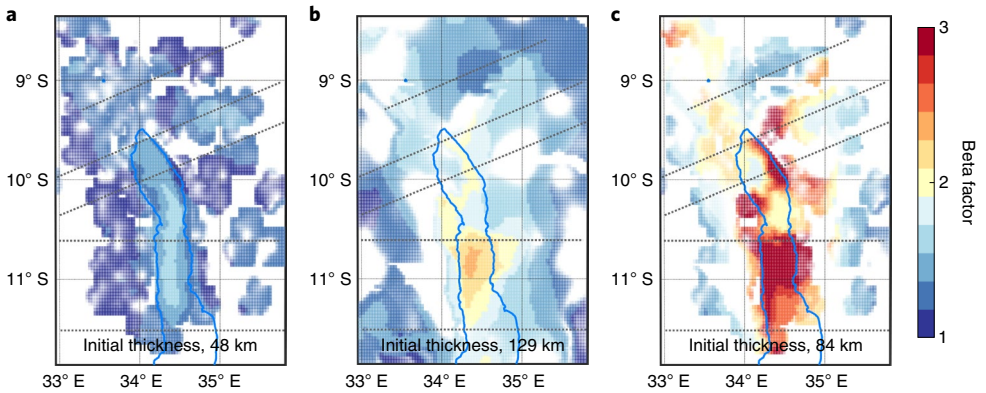


Fig. 3 | Stretching factor, beta (original thickness/current thickness). The assumed original thickness is noted in each panel. Contour map, beta values masked by s.d. (as in Fig. 2); grey lines, cross-section locations (Fig. 2); blue line, Lake Malawi. **a**, Crustal beta. The current crustal thickness is the difference between the topography (incorporating sedimentary basins in Lake Malawi[25]) and the Moho PVG. **b**, Lithospheric beta. The current lithospheric thickness is the difference between the topography and the LAB NVG. **c**, Lithospheric mantle beta. The current lithospheric mantle thickness is the difference between the Moho and the LAB. The mask is the maximum of **a** and **b**.

Additional NVGs interpreted as an intralithospheric structure are sometimes observed at shallower depths in our images (for example 80 ± 10 km depth east of 36° E (Fig. 2d)). Sp phases are better for the uppermost-mantle imaging (Fig. 2), whereas Ps, a higher-frequency phase, best images the Moho (Fig. 3 and Extended Data Fig. 1). We combine these results with absolute velocities from surface-wave tomography[14] and sediment thickness from three-dimensional (3D) refraction tomography[25] to constrain the thinning and modification of the lithosphere in the Malawi Rift.

Depth dependence of lithospheric alteration

We observe a striking shallowing of the LAB beneath the rift axis. Profile B–B′ (Fig. 2b) shows a smoothly varying NVG at 115 ± 10 km depth west of the rift upwarped to 65 ± 10 km just east of the central rift valley and deepening again to 105 ± 10 km east of the rift. Similar NVG geometries are also observed in profiles farther south beneath the Malawi Rift. We handpicked this phase on 0.1° spaced perpendicular cross-sections, which gave a map of the lithospheric thickness (for example, the white dotted lines in Fig. 2, and Extended Data Fig. 2). NVG amplitude is -0.05 ± 0.02, which corresponds to a sharp velocity drop of ~6%. Such velocity drops could be due to some combination of temperature, water content and grain size[26].

We handpicked a Moho on Ps images (for example, black dashed lines in Fig. 2, and Extended Data Fig. 2). A limited Moho topography across the rift is observed, compatible with previous passive-source imaging[27–29]. Deep basins within the rift lake[25] suggest a highly localized crustal thinning. We observe some substantial Moho upwarping at the edges of the surface expression of the rift (Fig. 2d and Extended Data Fig. 1b) to ~32 km, comparable to Moho topography beneath the adjacent Tanganyika Rift[30].

Mapping the ratio of the original thickness to the current thickness, beta, shows the distribution and extent of thinning[31]. Beta was calculated for the crust, lithosphere and lithospheric mantle to identify depth-dependent thinning (Fig. 3). For simplicity, we assumed that the prerift layer thickness is the maximum currently observed thickness of that layer in our study area (Methods). The crustal thinning is concentrated beneath Lake Malawi, with a maximum beta of $\sim 1.7 \pm 0.3$ (Fig. 3a). Whole-lithosphere thinning (ranging from 1.8 ± 0.3 to 2.3 ± 0.5 beneath the rift axis) is slightly greater than the crustal thinning and somewhat more distributed (Fig. 3b), comparable to that of the extent of the moderately slow uppermost mantle imaged tomographically[14,15]. The lithospheric mantle beneath Lake Malawi shows a much more pronounced thinning than that of the crust, with beta up to 3.8 ± 1.7 in the Central Basin (Fig. 3c)—more than twice that of the crust alone.

The observed strong depth dependence of thinning demonstrates that the Malawi Rift was not formed by a simple mechanical stretching[32]. Both crustal and mantle thinning are focused beneath the rift axis (Fig. 3) and the lower crust is strong[12], so crust–mantle decoupling cannot account for the observed depth dependence. Lithospheric-mantle thinning must be achieved by a combination of mechanical stretching and thermal and/or thermochemical alteration, weakening and perhaps removal. Thermal conduction alone is too slow to have weakened the lithosphere to this extent (Extended Data Fig. 3).

Localized melt injection would weaken the lithosphere[2,33], and we explore this within the limitation that the Malawi Rift appears melt-poor today. Although the Rungwe Volcanic Province (RVP, Fig. 1) northwest of Lake Malawi[7] has been volcanically active since 25 Ma (ref. [19]), volcanism and slow mantle shear-wave velocity (ν_S) anomalies are highly localized at the northern tip of the Malawi Rift[14,15]. Even the lowest regional uppermost-mantle shear velocities below the rift south of the RVP are high enough to preclude a strong thermal anomaly or substantial melt at present[14]. However, more melt may have been present in the past, and even small melt fractions may have substantial rheological impact. Recent work shows miniscule melt fractions (<0.2% melt) and/or near-solidus effects can lower mantle viscosity by 1–2 orders of magnitude[34,35]. Additionally, heat transport due to fluxing small-fraction (0.5%) melts can lower the solid viscosity by 40% (ref. [36]). If the lithospheric mantle contains pre-existing hydrated or pyroxenite-rich zones, partial melting and potential destabilization of the lithospheric mantle is possible with a modest heat input[37,38]. We propose that at the time of rift initiation, melt fractions may have sufficed to weaken the lithosphere and promote rifting that continues to the present; subsequently, the melt may have frozen, which led to negligible levels today.

Conceptual model of rifting in Malawi

We hypothesize that ancient lithospheric sutures provided a fertile environment for low-temperature, low-degree melting, and that these small-fraction melts systematically weakened the lithospheric mantle[39]. In the Malawi Rift, lithospheric thinning appears to follow pre-existing lithospheric heterogeneities (Figs. 1 and 3). Thinning is focused beneath the Ubendian Belt (North Basin) and its bounding suture with the Irumide Belt (Central Basin). The Ubendian Belt largely comprises amphibole-bearing gneisses with eclogites[40] and is associated with subduction as recently as the Neoproterozoic[41].

Content courtesy of Springer Nature, terms of use apply. Rights reserved

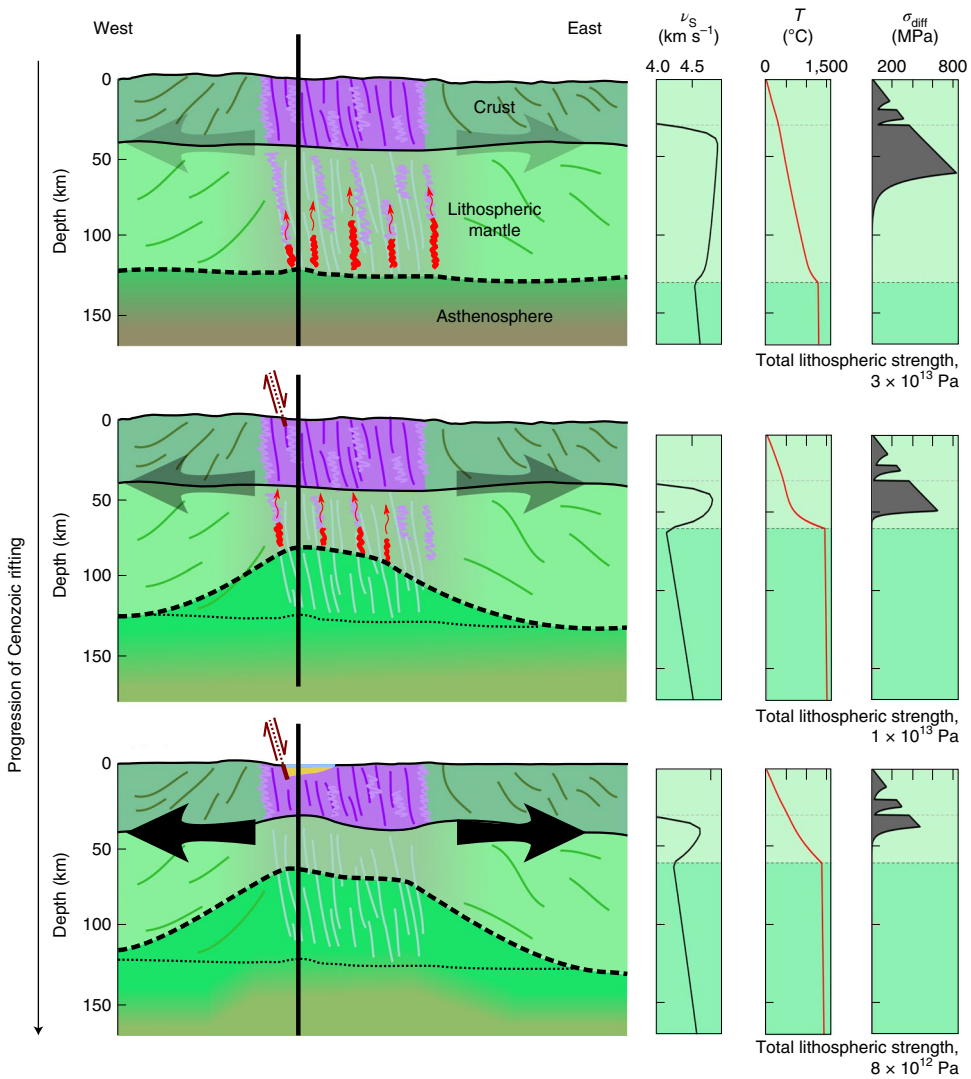


Fig. 4 | Possible evolution of the Malawi Rift. The left column shows a schematic of lithospheric evolution. Solid black line, Moho; thick dashed black line, rheological LAB; dotted black line, pre-rift LAB; black vertical line, location of the 1D profile in the right panels. Purple, Ubendian Belt (as in Fig. 1b); lighter purple wavy lines represent fusible heterogeneities; red wavy lines, partial melt; green lines, pre-existing fabric. The right columns show the calculated shear velocity (v_s), temperature (T) and yield strength (σ_{diff}) (Methods) from the evolving central part of the rift, calculated using the Very Broadband Rheology Calculator[50].

These compositions, and any pyroxenites formed by eclogite reacting with peridotite, have substantially lower melting temperatures than those of average mantle materials[42,43]. The Ubendian Belt has a history of weakness[10,40], as it has been repeatedly reactivated and magmatically intruded, and has a well-defined crustal structural grain that correlates with the trend of Cenozoic rifting[44].

Plume-influenced mantle may have impinged on the lithosphere and triggered the onset of volcanism in the RVP[19] and regional kimberlite intrusions[18] at ~30–25 Ma. This slightly hotter asthenosphere warms the lowermost lithospheric mantle and may initiate partial melting, particularly of fusible heterogeneities[40,41,45] in the lithosphere (Fig. 4, top row). RVP geochemistry suggests a plume-influenced source[46] with substantial lithospheric assimilation[7]. The slightly warmed, hydrated lithosphere is already prone to destabilize[47], and fluxing melts further weaken the lithosphere by heat advection[36] and chemical refertilization and/or rejuvenation[39]. The lithospheric mantle progressively weakens as melts rise (Fig. 4, middle row). The strong lithosphere is converted in situ to a mechanically weak asthenosphere, although the weak, relatively dense, altered lithospheric material may be partially removed[38,48] (Fig. 4, middle row). The remaining lithosphere warms conductively, weakening sufficiently to allow rifting (Fig. 4, bottom row).

North of Lake Malawi, the thinned lithosphere shifts northwest follow Karoo, Cretaceous and Palaeogene rifting[19], which may explain the localization of the RVP. Moving west towards the RVP from an area with a relatively uniform Moho and NVG (90–100 ± 10 km depth, profile A–A′; Fig. 2a), the NVG shallows slightly (80–85 ± 10 km depth, 33.8–34° E), but no uppermost mantle NVG is observed directly beneath the RVP (gap in the picked NVG around 9° S, 33.5° E; Fig. 3b and Extended Data Fig. 2b). This lithosphere may be so thermally or chemically modified or eroded that little to no high-velocity lid remains, compatible with low shear velocities here, which extend up to the Moho[14], and the substantial lithospheric mantle component of erupted lavas[6,7].

Given the relatively high average asthenospheric shear velocities (4.35 ± 0.1 km s^{-1}) (ref. [14]) in the region now, this model requires a temporal decrease in melt fraction during the up to 25 Ma history of this rift system. This reduction would arise naturally if the melts are

Content courtesy of Springer Nature, terms of use apply. Rights reserved

largely sourced in finite fusible compositional heterogeneities, such as eclogites and pyroxenites[42,43]. Any magmatic addition to the crust would bias our crustal beta to be too low. However, the observed lithospheric thinning is not expected to generate substantial volumes of melt (Methods and Extended Data Fig. 4), so we expect this effect to be small.

Alternatively, very small melt fractions may persist in the system. This would require the macroscopic rheological effects of very small melt fractions to be even greater than previously believed compared with the effects on seismic velocity. This scenario would still require melting at low (flux-induced) temperatures[14].

Implications for magma-poor rifting worldwide

Substantial lithospheric thinning appears to have occurred beneath the early stage Malawi Rift. The thinning is localized beneath the rift axis and is much stronger within the mantle lithosphere than within the crust. This requires some process beyond mechanical stretching, perhaps alteration or thermal and/or thermochemical erosion of the lithospheric root. However, local tomographic results imply subsolidus conditions and negligible melt in and beneath the lithosphere at present. As such, the system has probably evolved from one with a finite amount of melt to the melt-free conditions inferred today.

Compositional and/or rheological heterogeneities associated with ancient sutures and metasomatism may control the magnitude of low-degree melting and/or induced localization. In the Malawi Rift, lithospheric thinning follows the Ubendian Belt. Such lithospheric mantle scarring is increasingly incorporated into geodynamic models as the driver of localized deformation[49] and should be considered in evaluating other rifts.

These new constraints on localized lithospheric thinning in an active, early-stage magma-poor rift have wide-ranging implications for our understanding of mature rifts and passive-rifted margins worldwide. At ancient margins, lithospheric stretching can only be inferred from subsidence, which is often uncertain due to a paucity of drilling constraints and uncertainty in parameters such as palaeowater depth and the density of deep sediments. Here we present observations that localized lithospheric extension is occurring in an active, magma-poor rift system. More fundamentally, these results demonstrate that substantial, focused lithospheric modification and thinning can occur even in the absence of substantially elevated temperatures and abundant melt. The weakening of the mantle lithospheric root here occurred very early in this early-stage continental rift, which suggests that the much-debated problem of how to rift thick lithosphere should perhaps focus on the preferential weakening and destruction of the lithospheric mantle root rather than on how to rift intact lithosphere.

Online content

Any methods, additional references, Nature Research reporting summaries, source data, extended data, supplementary information, acknowledgements, peer review information; details of author contributions and competing interests; and statements of data and code availability are available at https://doi.org/10.1038/s41561-020-0609-y.

Received: 21 November 2019; Accepted: 3 June 2020;
Published online: 20 July 2020

References

1. Forsyth, D. & Uyeda, S. On the relative importance of the driving forces of plate motion. *Geophys. J. Int.* **43**, 163–200 (1975).
2. Buck, W. R. in *Rheology and Deformation of the Lithosphere at Continental Margins* (eds Karner, G. D. et al.) 1–30 (Columbia Univ. Press, 2004).
3. Versfelt, J. & Rosendahl, B. R. Relationships between pre-rift structure and rift architecture in Lakes Tanganyika and Malawi, East Africa. *Nature* **337**, 354–357 (1989).
4. Celli, N. L., Lebedev, S., Schaeffer, A. J. & Gaina, C. African cratonic lithosphere carved by mantle plumes. *Nat. Commun.* **11**, 92 (2020).
5. Wang, H., van Hunen, J. & Pearson, D. G. The thinning of subcontinental lithosphere: the roles of plume impact and metasomatic weakening. *Geochem. Geophys. Geosyst.* **16**, 1156–1171 (2015).
6. Rooney, T. O. The Cenozoic magmatism of East Africa: part V—magma sources and processes in the East African Rift. *Lithos* **360–361**, 105296 (2020).
7. Furman, T. Geochemistry of East African Rift basalts: an overview. *J. Afr. Earth Sci.* **48**, 147–160 (2007).
8. Bastow, I. D., Nyblade, A. A., Stuart, G. W. & Rooney, T. O. Upper mantle seismic structure beneath the Ethiopian hot spot: rifting at the edge of the African low-velocity anomaly. *Geochem. Geophys. Geosyst.* **9**, Q12022 (2008).
9. Chorowicz, J. The East African rift system. *J. Afr. Earth Sci.* **43**, 379–410 (2005).
10. Hanson, R. E. in *Proterozoic East Gondwana: Supercontinent Assembly and Breakup* Special Publications 206 (eds Yoshida, M. et al.) 427–463 (The Geological Society, 2003).
11. Ebinger, C. J., Jackson, J. A., Foster, A. N. & Hayward, N. J. Extensional basin geometry and the elastic lithosphere. *Philos. Trans. R. Soc. Lond. A* **357**, 741–765 (1999).
12. Craig, T. J., Jackson, J. A., Priestley, K. & Mckenzie, D. Earthquake distribution patterns in Africa: their relationship to variations in lithospheric and geological structure, and their rheological implications. *Geophys. J. Int.* **185**, 403–434 (2011).
13. O'Donnell, J. P., Adams, A., Nyblade, A. A., Mulibo, G. D. & Tugume, F. The uppermost mantle shear wave velocity structure of eastern Africa from Rayleigh wave tomography: constraints on rift evolution. *Geophys. J. Int.* **194**, 961–978 (2013).
14. Accardo, N. J. et al. Thermo-chemical modification of the upper mantle beneath the Northern Malawi Rift constrained from shear velocity imaging. *Geochem. Geophys. Geosyst.* **21**, e2019GC008843 (2020).
15. Grijalva, A. et al. Seismic evidence for plume- and craton-influenced upper mantle structure beneath the Northern Malawi Rift and the Rungwe Volcanic Province, East Africa. *Geochem. Geophys. Geosyst.* **19**, 3980–3994 (2018).
16. Sarafian, E. et al. Imaging Precambrian lithospheric structure in Zambia using electromagnetic methods. *Gondwana Res.* **54**, 38–49 (2018).
17. Lavayssiere, A. et al. Imaging lithospheric discontinuities beneath the northern East African Rift using S-to-P receiver functions. *Geochem. Geophys. Geosyst.* **19**, 4048–4062 (2018).
18. Ebinger, C. J. & Scholz, C. A. in *Tectonics of Sedimentary Basins: Recent Advances* (eds Busby, C. & Azor, A.) 185–208 (Wiley-Blackwell, 2012).
19. Roberts, E. M. et al. Initiation of the Western Branch of the East African Rift coeval with the eastern branch. *Nat. Geosci.* **5**, 289–294 (2012).
20. Stamps, D. S., Saria, E. & Kreemer, C. A geodetic strain rate model for the East African Rift system. *Sci. Rep.* **8**, 732 (2018).
21. Scholz, C. A. et al. Intrarift fault fabric, segmentation, and basin evolution of the Lake Malawi (Nyasa) Rift, East Africa. *Geosphere* (in the press).
22. Shillington, D. J. et al. Acquisition of a unique onshore/offshore geophysical and geochemical dataset in the Northern Malawi (Nyasa) Rift. *Seismol. Res. Lett.* **87**, 1406–1416 (2016).
23. Fischer, K. M. in *Treatise on Geophysics* 2nd edn, Vol. 1 (ed. Schubert, G.) 587–612 (Elsevier, 2015).
24. Wölbern, I., Rümpker, G., Link, K. & Sodoudi, F. Melt infiltration of the lower lithosphere beneath the Tanzania craton and the Albertine rift inferred from S receiver functions. *Geochem. Geophys. Geosyst.* **13**, Q0AK08 (2012).
25. Accardo, N. J. et al. Constraints on rift basin structure and border fault growth in the Northern Malawi Rift from 3D seismic refraction imaging. *J. Geophys. Res. Solid Earth* **123**, 10003–10025 (2018).
26. Hopper, E. & Fischer, K. M. The changing face of the lithosphere–asthenosphere boundary: imaging continental scale patterns in upper mantle structure across the contiguous U.S. with Sp converted waves. *Geochem. Geophys. Geosyst.* **19**, 2593–2614 (2018).
27. Borrego, D. J. et al. Crustal structure surrounding the northern Malawi Rift and beneath the Rungwe Volcanic Province, East Africa. *Geophys. J. Int.* **215**, 14140–1426 (2018).
28. Njinju, E. A. et al. Lithospheric structure of the Malawi Rift: implications for magma-poor rifting processes. *Tectonics* **38**, 3835–3853 (2019).
29. Kachingwe, M., Nyblade, A. & Julià, J. Crustal structure of Precambrian terranes in the southern African subcontinent with implications for secular variation in crustal genesis. *Geophys. J. Int.* **202**, 533–547 (2015).
30. Hodgson, I. et al. Crustal structure at a young continental rift: a receiver function study from the Tanganyika Rift. *Tectonics* **36**, 2806–2822 (2017).
31. Davis, M. & Kusznir, N. in *Rheology and Deformation of the Lithosphere* (eds Karner, G. D. et al.) 92–137 (Columbia Univ. Press, 2004); https://doi.org/10.7312/karn12738-005
32. McKenzie, D. Some remarks on the development of sedimentary basins. *Earth Planet. Sci. Lett.* **40**, 25–32 (1978).
33. Stamps, D. S., Flesch, L. M., Calais, E. & Ghosh, A. Current kinematics and dynamics of Africa and the East African Rift System. *J. Geophys. Res. Solid Earth* **119**, 5161–5186 (2014).

Content courtesy of Springer Nature, terms of use apply. Rights reserved

34. Holtzman, B. K. Questions on the existence, persistence, and mechanical effects of a very small melt fraction in the asthenosphere. *Geochem. Geophys. Geosyst.* **17**, 470–484 (2016).
35. Takei, Y. Effects of partial melting on seismic velocity and attenuation: a new insight from experiments. *Annu. Rev. Earth Planet. Sci.* **45**, 447–470 (2017).
36. Schmeling, H. & Wallner, H. Magmatic lithospheric heating and weakening during continental rifting: a simple scaling law, a 2D thermomechanical rifting model and the East African Rift System. *Geochem. Geophys. Geosyst.* **13**, Q08001 (2012).
37. Phipps Morgan, J. Thermodynamics of pressure release melting of a veined plum pudding mantle. *Geochem. Geophys. Geosyst.* **2**, 2000GC000049 (2001).
38. Furman, T., Nelson, W. R. & Elkins-Tanton, L. T. Evolution of the East African rift: drip magmatism, lithospheric thinning and mafic volcanism. *Geochim. Cosmochim. Acta* **185**, 418–434 (2016).
39. Roy, M. et al. Macroscopic coupling of deformation and melt migration at continental interiors, with applications to the Colorado Plateau. *J. Geophys. Res. Solid Earth* **121**, 3762–3781 (2016).
40. Lenoir, J. L., Liegeois, J.-P., Theunissen, K. & Klerkx, J. The Palaeoproterozoic Ubendian shear belt in Tanzania: geochronology and structure. *J. Afr. Earth Sci.* **19**, 169–184 (1995).
41. Boniface, N. & Schenk, V. Neoproterozoic eclogites in the Paleoproterozoic Ubendian Belt of Tanzania: evidence for a pan-African suture between the Bangweulu Block and the Tanzania Craton. *Precambrian Res.* **208–211**, 72–89 (2012).
42. Yaxley, G. M. Experimental study of the phase and melting relations of homogeneous basalt + peridotite mixtures and implications for the petrogenesis of flood basalts. *Contrib. Mineral. Petrol.* **139**, 326–338 (2000).
43. Hacker, B. R. & Abers, G. A. Subduction Factory 3: an Excel worksheet and macro for calculating the densities, seismic wave speeds, and H_2O contents of minerals and rocks at pressure and temperature. *Geochem. Geophys. Geosyst.* **5**, Q01005 (2004).
44. Wheeler, W. H. & Karson, J. A. Structure and kinematics of the Livingstone Mountains border fault zone, Nyasa (Malawi) Rift, southwestern Tanzania. *J. Afr. Earth Sci.* **8**, 393–413 (1989).
45. Mana, S., Furman, T., Turrin, B. D., Feigenson, M. D. & Swisher, C. C. III Magmatic activity across the East African North Tanzanian divergence zone. *J. Geol. Soc. Lond.* **172**, 368–389 (2015).
46. Hilton, D. R. et al. Helium isotopes at Rungwe Volcanic Province, Tanzania, and the origin of East African Plateaux. *Geophys. Res. Lett.* **38**, L21304 (2011).
47. Liao, J., Wang, Q., Gerya, T. & Ballmer, M. D. Modeling craton destruction by hydration-induced weakening of the upper mantle. *J. Geophys. Res. Solid Earth* **122**, 7449–7466 (2017).
48. Holtzman, B. K. & Kendall, J. M. Organized melt, seismic anisotropy, and plate boundary lubrication. *Geochem. Geophys. Geosyst.* **11**, Q0AB06 (2010).
49. Heron, P. J., Pysklywec, R. N. & Stephenson, R. in *Fifty Years of the Wilson Cycle Concept in Plate Tectonics* Special Publications 470 (eds Wilson, R. W. et al.), 137–155 (The Geological Society, 2018).
50. Holtzman, B. K. & Havlin, C. *The Very Broadband Rheology Calculator* (2020); https://vbr-calc.github.io/vbr/

Publisher's note Springer Nature remains neutral with regard to jurisdictional claims in published maps and institutional affiliations.

© The Author(s), under exclusive licence to Springer Nature Limited 2020

Content courtesy of Springer Nature, terms of use apply. Rights reserved

Methods

Converted-wave imaging of the Malawi Rift lithosphere. This study uses both Ps and Sp converted waves, although we focused primarily on the uppermost mantle structure revealed by the Sp imaging. These waves are generated at relatively sharp impedance contrasts (for example, a 5% velocity change over <50 km) (refs [51,52]). Sp waves have been used extensively to study the lithospheric structure as the converted wave precedes the parent S wave, which avoids the contamination by crustal and sedimentary multiples in Ps imaging. However, the relatively low signal-to-noise ratio of these phases requires a dense data coverage for reliable interpretations; as such, the SEGMeNT dataset provides an opportunity for a detailed imaging of the Lake Malawi rift by Sp waves.

Ps waves are commonly used to map crustal thickness. Few local studies exist[27,29,53,54], although a separate SEGMeNT study is focused entirely on Ps receiver functions (RFs) and joint inversion with surface wave dispersion[27]. These land-based studies are remarkable in finding negligible variation in crustal thickness near the rift, despite the strong upper crustal expression of the rift valleys. Averaged by terrane, crustal thickness varies from 39 to 42 km. However, preliminary results from the inversion of active source data collected in Lake Malawi[55] suggest a substantially thinner crust, 32 km.

Data. We collected all the available data from local broadband stations for earthquakes with $M_w > 5.8$ as reported in the United States Geological Survey National Earthquake Information Center since 1994. This data was obtained from the Incorporated Research Institutions for Seismology Data Management Center. We used data from 74 broadband stations, which included 59 stations from the SEGMeNT experiment (deployed 2013–2015). This includes five seismometers deployed in Lake Malawi itself. Although the data quality was insufficient to obtain interpretable single-station observations directly beneath the lake, we include the best data from these stations in our final stack. We also used 13 stations from the SAFARI experiment (deployed 2012–2014, https://doi.org/10.7914/SN/XK_2012), and two permanent Africa Array stations (https://doi.org/10.7914/SN/AF). We excluded sources deeper than 300 km and outside the distance range 55–85° to avoid spurious interpretations of other teleseismic phases and postcritical waveforms.

We calculated both Ps and Sp RF stacks for this dataset. Given the relatively sparse data coverage, we had to carefully cull the Sp dataset, which has an intrinsically lower signal-to-noise ratio than that of the Ps dataset. We previously found that including all the data produces a better final image[26], but that requires sufficient data in the stack to cancel out the noise. We culled the dataset by lightly filtering the data and examining each component by eye for a good signal-to-noise ratio, strong similarity to other waveforms from the same earthquake and lack of instrumental artefacts.

In total, we calculated 820 Sp RFs, and 3,001 Ps RFs (Extended Data Fig. 5). The data coverage is fair, although the back azimuthal distribution of the Sp dataset (Extended Data Fig. 5a) means that the eastern side of the rift is better imaged than the western side. Comparison of Extended Data Fig. 6a,b clearly demonstrates how the shallower ray paths and deeper depths of interest of the Sp stack result in markedly different data distribution to that of the Ps stack. In particular, Ps imaging does not cover the rift beneath Lake Malawi very well. However, we have many stations on both shores of the (narrow) lake, so any Moho topography we are missing would have to be very sharp (<40 km wide). Many lakeshore stations can resolve crustal thinning, particularly in the Central Basin (Extended Data Fig. 5), which is of a magnitude similar to that estimated from preliminary results of a refraction survey in Lake Malawi[55]. Additionally, the majority of the crustal thinning reported in this study is due to sedimentary basins beneath Lake Malawi, which were well imaged by Accardo et al.[25]. In this study, we chose to show colocated Ps and Sp stacks to facilitate comparison, although this does mean the data distribution is suboptimal in some profiles.

Waveform processing. We rotated the data into P and horizontal polarization components using a free-surface transfer matrix[56,57], with values of P-wave velocity $(\nu_P)/\nu_S$ for each station found by a grid search to minimize the daughter P wave amplitude on the parent horizontal polarization component[52]. The greater shear attenuation of teleseismic waves means that Sp waves have a lower frequency content than Ps waves. For Sp, we filtered the waveforms between 4 and 100 s, which minimized interferences between the lithospheric phases and processing artefacts[52,58]. For Ps, we filtered between 1 and 100 s. This gave a dominant period for S waves of ~9 s and for P waves of ~2 s. RFs can resolve to wavelength/2 (refs [59,60]), so for the regional average crustal ν_P of 6.5 km s^{-1} (ref. [27]) and average upper mantle ν_S of 4.5 km s^{-1} (ref. [14]; our depths are accurate to ±3 km for Ps and ±10 km for Sp).

We deconvolved using the extended-time multitaper cross-correlation method[61]. We converted the waveforms from time to depth using a station-specific velocity model extracted from the local surface-wave tomography of Accardo et al.[14], but excluded the depths below which the converted wave would be postcritical. This shear-velocity model uses local Moho constraints from Borrego et al.[27] that are broadly similar to our own except for short-wavelength deviations at a few stations and seeing limited topography beneath the rift axis. The latter does not overly concern us as an assumed Moho that is too deep will act to steepen the overall calculated ray path (increasing the apparent depth for a given observed differential travel time) and slow the overall velocity (decreasing the apparent depth) such that the total effect is small (±0.5 km change in the calculated LAB depth for a 5 km change in the Moho depth; Extended Data Fig. 6).

We used common-conversion point stacking to generate a 3D image and smoothed the data according to a Fresnel zone appropriate for the dominant period of these waves, 9 and 2 s for Sp and Ps, respectively (Lekić et al.[62]). Finally, phase polarities of the Sp stack were reversed for consistency with the Ps imaging. A positive phase was generated by a PVG with depth, and a negative phase by a NVG with depth.

We used a constant ν_P/ν_S (1.75, consistent with crustal estimates from H–κ stacking[27]) to convert the local ν_S model[14] into ν_P for the purposes of migration. Crustal multiples in the Ps-converted waves can be used to constrain the ν_P/ν_S ratios of the whole crust[27,63], but this is difficult to implement in a meaningful way in a common-conversion point stack with our data coverage. As such, we may not capture the depth variation completely, but the uncertainty in depth variation associated with a reasonable range of ν_P/ν_S is small compared with the variations we interpret as the path and velocity effects largely cancel each other out (±2 km change in the calculated LAB depth given for ν_P/ν_S that ranges from 1.7 to 1.85 throughout the model; Extended Data Fig. 6).

Phase picking. To generate the depth maps, we hand-picked phases on cross-sections at a 0.1° spacing that ran both north–south and east–west across the study region. The hand-picked depths were used to guide an automated picker searching for maximum amplitude phases to within 10 km of the desired phase. Any overlapping picks from the perpendicular sections that did not match were removed, as were any picks below a threshold amplitude (0.02).

Generating beta maps. In this exercise, we wanted to ensure we obtained conservative estimates of differential thinning between the crust and lithospheric mantle, so some of the chosen parameters are perhaps not the most realistic. We used an initial crustal thickness of 48 km, the thickest observed present-day crust in the study region (east of the north Central Basin), similar to estimates of maximum crustal thickness across Africa[64]. Although it is unlikely that the crust was everywhere this thick, using this value maximizes the apparent crustal thinning. We used an initial total lithospheric thickness of 129 km, similarly the thickest currently observed in the study region (east of the south Central Basin). Given this currently observed lithospheric thickness and the age and stability of the lithosphere in central East Africa (150–240 km (refs [13,16,65] and >280 km in the Tanzanian Craton[65]), 130 km is probably an underestimate. Thus, using this value gives a minimum amount of lithospheric thinning. As such, the difference between thinning of the crust (calculated beta ≤1.7; beta for the initial crustal thickness of 40 km is ≤1.4) and the lithospheric mantle (calculated beta ≤3.8; beta for initial lithospheric mantle thickness of 150 km is ≤6.8) is probably even more extreme than we have shown here.

From the automated phase picks, we generated an interpolated surface of the depth to the Moho and LAB. For the Moho Ps imaging, sparse coverage beneath the lake itself means that a simple interpolation from largely land-based Ps observations would probably underestimate the amount of Moho upwarp (that is, crustal thinning). To maximize the estimated crustal beta, we took the shallowest Moho depth imaged on the lakeshore (32.5 km), artificially added a sequence of points in the centre of the lake with this depth and then interpolated the Moho surface. This region of assigned Moho depths is not masked in the mapped figures (Fig. 3 and Extended Data Fig. 2). To obtain the crustal thickness, we took the difference between the topography and the Moho surface, with the basement topography beneath Lake Malawi taken as the inferred base of the syn-rift sedimentary basins[25]. To calculate beta, we divided the current observed crustal thickness across the region by the maximum local crustal thickness, 48 km. This thick crust is only imaged over a small area beneath the eastern rift flank, and it is likely that the original regional crustal thickness was closer to the present local average crustal thickness of 40 km given the average crustal thickness in Africa[64] and in stable continental settings globally (38 ± 4 km (ref. [66])). However, we chose to use this maximum value, which probably preserves some pre-existing Moho topography, to maximize our estimate of crustal beta.

For the LAB, we made an interpolated surface of the depth to the Sp observations interpreted as the LAB. Data coverage beneath the lake is much better for Sp than Ps waves (Extended Data Fig. 5), so we only used Sp observations to make this interpolated surface. For lithospheric beta, we used the difference between the crustal topography and LAB surface; for mantle lithospheric beta, we used the difference between the Moho and LAB surfaces. In this case, we also chose the maximum currently observed local lithospheric (or lithospheric mantle) thickness to calculate beta, 129 km (84-km-thick lithospheric mantle). In this case, the original lithospheric thickness of this cratonic region is likely to have been much thicker than 129 km; indeed, it is estimated to be at least 150–200 km thick just outside of our study region[13,16]. In this small study region, the whole lithosphere appears to have been thinned. However, by using the relatively thin maximum observed lithospheric thickness, we minimized our calculated estimates of lithospheric and lithospheric mantle thinning.

In the plots (Fig. 3 and Extended Data Fig. 2), we mask picks according to s.d. of the RF observations. We also mask by proximity to pick locations (at best, spaced 0.1° apart), such that we do not show large areas of pure interpolation. Map

Content courtesy of Springer Nature, terms of use apply. Rights reserved

locations more than 0.25° from a picked phase depth are completely transparent. The only exception is the crustal thickness beneath Lake Malawi, which we do not mask as the Moho depth here is largely derived from the assigned value of 32.5 km. When comparing two interpolated surfaces (that is, the Moho and LAB, to obtain lithospheric mantle thickness), the opacity of the mask is based on the less well-imaged surface at that location.

Conditions in our model of Malawi Rift evolution. The three right-most columns of Fig. 4 plot conditions calculated at various points during the hypothesized evolution of the Malawi Rift. We started with an equilibrium geotherm for a 130-km-thick lithosphere and use a finite-difference model to calculate how it evolves through time as the base of the lithosphere is removed. The lithosphere was eroded from an initial thickness of 130 km (chosen to match observations of the thickest lithosphere in the study region today) to one of 60 km chosen to match the thinnest lithosphere in the study region today) by removal of the base of the lithosphere at a rate of 5 km Ma^{-1}. Havlin et al.[67] calculated reasonable thinning velocities of 1–6 km Ma^{-1} driven by melt infiltration at the base of the lithosphere, and their most recent calculations indicate this cap might be even higher (16 km Ma^{-1}). The thinning occurs by heating and weakening lithospheric mantle material to the point that it becomes mechanically indistinguishable from the asthenosphere by raising it to the temperature of the dry solidus. Here, our assumed thermal perturbation is enough to raise the lithosphere above the 'plum solidus' of a pyroxenite-laden lherzolite[37], and hence we simply imposed this thinning of the rheological lithosphere in our calculations of the geotherm. Furthermore, we disregarded any effects of heat advection via percolation of partial melts into the shallower lithospheric mantle, which gave us an endmember estimate of weakening due to basal erosion alone. Using the Very Broadband Rheology Calculator[34,50,68], we calculated the expected ν_S values, including anelastic effects for these geotherms. We also used these to calculate a yield-strength envelope for the lithosphere, with the following parameterizations: Tokle et al.[69] for a wet quartz upper crust, Rybacki et al.[70] for a dry anorthosite lower crust and Hirth and Kohlstedt[71] for a dry olivine upper mantle. We chose these dry rheological laws to give the most conservative estimates of lithospheric strength. In reality, both fusible heterogeneities embedded in the lithosphere and heat advection by rising melts are likely to make the lithosphere easier to rift.

Expected partial melting from lithospheric thinning. Surface volcanism in the Malawi Rift region is limited to the RVP, so any model for the evolution of the rift cannot involve the generation of large melt fractions. We calculated the expected melt fraction in a 1D column for a range of mantle potential temperatures and crustal beta factors using the Katz parametrization[72] to quantify passive decompression melting of anhydrous mantle peridotite with 15 wt% clinopyroxene[73]. For simplicity, we ignored the small-fraction pyroxenite melts. We assumed that stretching is strongly depth dependent, as suggested by our observations, with twice as much extension of the lithospheric mantle. We used an initial crustal thickness of 48 km (density, 2,800 kg m^{-3}) and an initial lithospheric thickness of 129 km (density, 3,300 kg m^{-3}). These thicknesses are from our assumed original layer thicknesses in the beta factor calculations. Changing the initial crustal thickness (for example, to 40 km) does not make a substantial difference in our calculations. Integrated partial melt fractions were converted into the thickness of the generated igneous material that was added to the crust. For normal asthenospheric potential temperatures (1,300–1,350 °C), we expect no more than 2 km of igneous material to be generated for the observed crustal beta factors of ≤1.7 (Extended Data Fig. 4).

Data availability

The seismic data were obtained from the Incorporated Research Institutions for Seismology Data Management Center. We used data from the SEGMeNT (https://doi.org/10.7914/SN/YQ_2013), SAFARI (https://doi.org/10.7914/SN/XK_2012), and Africa Array stations (https://doi.org/10.7914/SN/AF) networks.

Code availability

RF codes (written in MATLAB) are freely available from the corresponding author.

References

51. Ford, H. A., Fischer, K. M., Abt, D. L., Rychert, C. A. & Elkins-Tanton, L. T. The lithosphere–asthenosphere boundary and cratonic lithospheric layering beneath Australia from Sp wave imaging. *Earth Planet. Sci. Lett.* **300**, 299–310 (2010).
52. Mancinelli, N. J. & Fischer, K. M. The spatial sensitivity of Sp converted waves–scattered wave kernels and their applications to receiver-function migration and inversion. *Geophys. J. Int.* **212**, 1722–1735 (2017).
53. Tugume, F., Nyblade, A. & Julia, J. Moho depths and Poisson's ratios of Precambrian crust in East Africa: evidence for similarities in Archean and Proterozoic crustal structure. *Earth Planet. Sci. Lett.* **356**, 73–81 (2012).
54. Last, R. J., Nyblade, A. A., Langston, C. A. & Owens, T. J. Crustal structure of the East African Plateau from receiver functions and Rayleigh wave phase velocities. *J. Geophys. Res. Solid Earth* **102**, 24469–24483 (1997).
55. Shillington, D. J. et al. Intrabasin faults accommodate significant cumulative and recent extension in the early stage Malawi Rift, East Africa. In *2018 AGU Fall Meeting* Abstract T13F-0267 (American Geophysical Union, 2018).
56. Kennett, B. L. N. The removal of free surface interactions from three-component seismograms. *Geophys. J. Int.* **104**, 153–163 (1991).
57. Bostock, M. G. Mantle stratigraphy and evolution of the Slave province. *J. Geophys. Res. Solid Earth* **103**, 21183–21200 (1998).
58. Hopper, E., Ford, H. A., Fischer, K. M., Lekic, V. & Fouch, M. J. The lithosphere-asthenosphere boundary and the tectonic and magmatic history of the northwestern United States. *Earth Planet. Sci. Lett.* **402**, 69–81 (2014).
59. Bostock, M. G. Seismic imaging of lithospheric discontinuities and continental evolution. *Lithos* **48**, 1–16 (1999).
60. Rychert, C. A., Rondenay, S. & Fischer, K. M. P-to-S and S-to-P imaging of a sharp lithosphere–asthenosphere boundary beneath eastern North America. *J. Geophys. Res.* **112**, B08314 (2007).
61. Helffrich, G. Extended-time multitaper frequency domain cross-correlation receiver-function estimation. *Bull. Seismol. Soc. Am.* **96**, 344–347 (2006).
62. Lekić, V., French, S. W. & Fischer, K. M. Lithospheric thinning beneath rifted regions of southern California. *Science* **334**, 783–787 (2011).
63. Zhu, L. & Kanamori, H. Moho depth variation in southern California. *J. Geophys. Res.* **105**, 2969–2980 (2000).
64. Tedla, G. E., van der Meijde, M., Nyblade, A. A. & Van der Meer, F. D. A crustal thickness map of Africa derived from a global gravity field model using Euler deconvolution. *Geophys. J. Int.* **187**, 1–9 (2011).
65. Priestley, K. & McKenzie, D. The thermal structure of the lithosphere from shear wave velocities. *Earth Planet. Sci. Lett.* **244**, 285–301 (2006).
66. Laske, G., Ma, Z., Masters, G. & Pasyanos, M. E. *Crust 1.0: A New Global Crustal Model at 1×1 Degrees* (2020); https://igppweb.ucsd.edu/~gabi/crust1.html
67. Havlin, C., Parmentier, E. M. & Hirth, G. Dike propagation driven by melt accumulation at the lithosphere–asthenosphere boundary. *Earth Planet. Sci. Lett.* **376**, 20–28 (2013).
68. Bellis, C. & Holtzman, B. K. Sensitivity of seismic measurements to frequency-dependent attenuation and upper mantle structure: an initial approach. *J. Geophys. Res. Solid Earth* **119**, 5497–5517 (2014).
69. Tokle, L., Hirth, G. & Behr, W. M. Flow laws and fabric transitions in wet quartzite. *Earth Planet. Sci. Lett.* **505**, 152–161 (2019).
70. Rybacki, E., Gottschalk, M., Wirth, R. & Dresen, G. Influence of water fugacity and activation volume on the flow properties of fine-grained anorthite aggregates. *J. Geophys. Res. Solid Earth* **111**, B03203 (2006).
71. Hirth, G. & Kohlstedt, D. L. Rheology of the upper mantle and the mantle wedge: a view from the experimentalists. *Geophys. Monogr.* **138**, 83–105 (2003).
72. Katz, R. F., Spiegelman, M. & Langmuir, C. H. A new parameterization of hydrous mantle melting. *Geochem. Geophys. Geosyst.* **4**, 1073 (2003).
73. Davis, J. K. & Lavier, L. L. Influences on the development of volcanic and magma-poor morphologies during passive continental rifting. *Geosphere* **13**, 1524–1540 (2017).

Acknowledgements

We thank R. Marzen for calculating partial melt fractions and C. Ebinger for her comments on this manuscript and her contributions to the SEGMeNT project in general. Funding for this work was provided by the NSF Continental Dynamics Program, with grants EAR-1110921, 1109293 and 1110882.

Author contributions

E.H. processed and analysed the data and wrote the bulk of the manuscript. J.B.G. and D.J.S. oversaw the project and were instrumental in developing the conceptual model. N.J.A. carried out the surface wave analysis integral to understanding these results and contributed to the manuscript. A.A.N. contributed to discussions and editing of the manuscript. B.K.H. and C.H. provided access to the Very Broadband Rheology code and were involved in discussions on its application, as well as contributing to the broader conceptions of the role of melt discussed in the manuscript. J.B.G., D.J.S., N.J.A., A.A.N., C.A.S., P.R.N.C., R.W.F., G.D.M. and G.M. were heavily involved in collecting the SEGMeNT dataset and discussions to place these results in a broader context.

Competing interests

The authors declare no competing interests.

Additional information

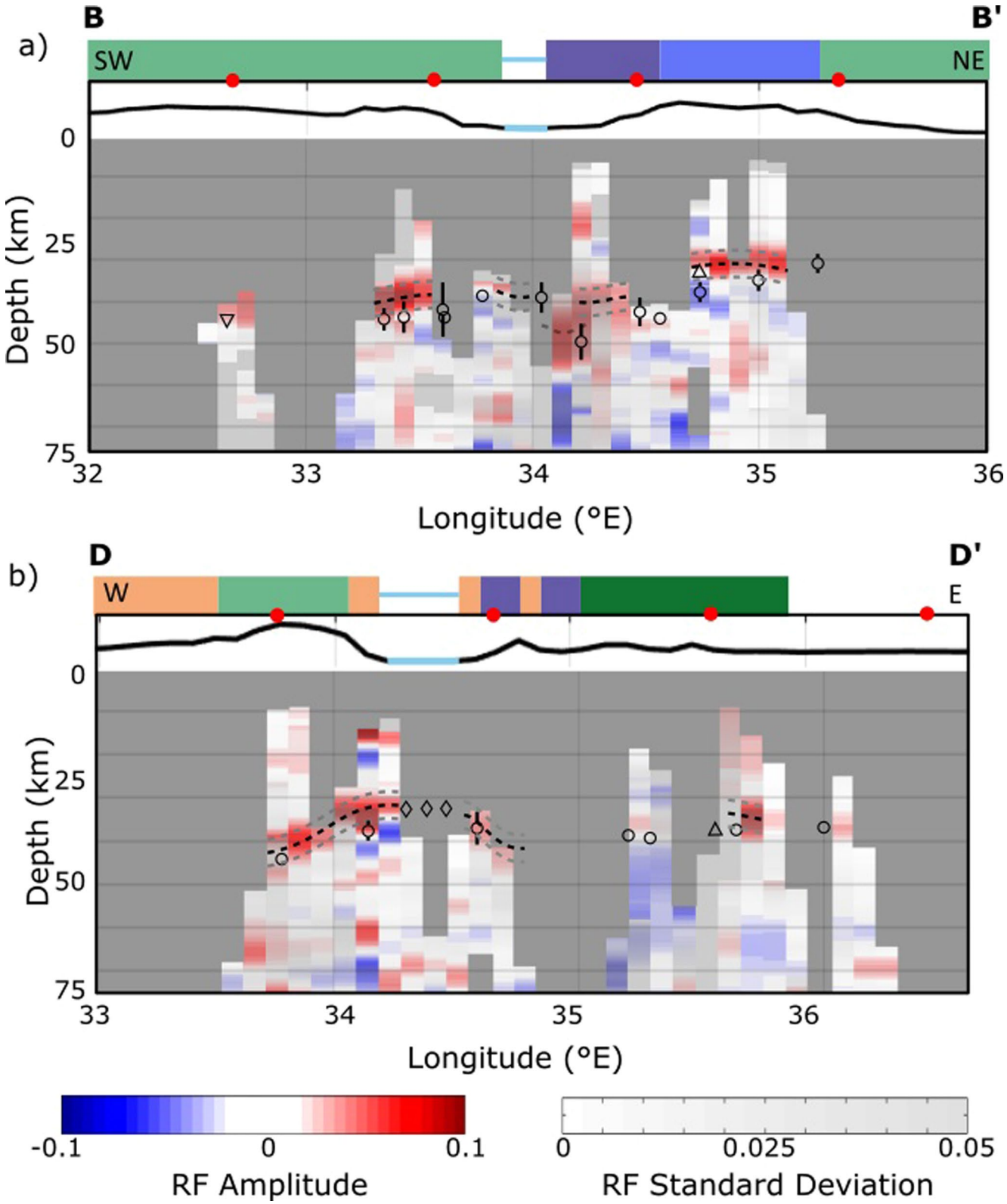
Extended data is available for this paper at https://doi.org/10.1038/s41561-020-0609-y.

Correspondence and requests for materials should be addressed to E.H.

Peer review information Primary Handling Editor: Stefan Lachowycz.

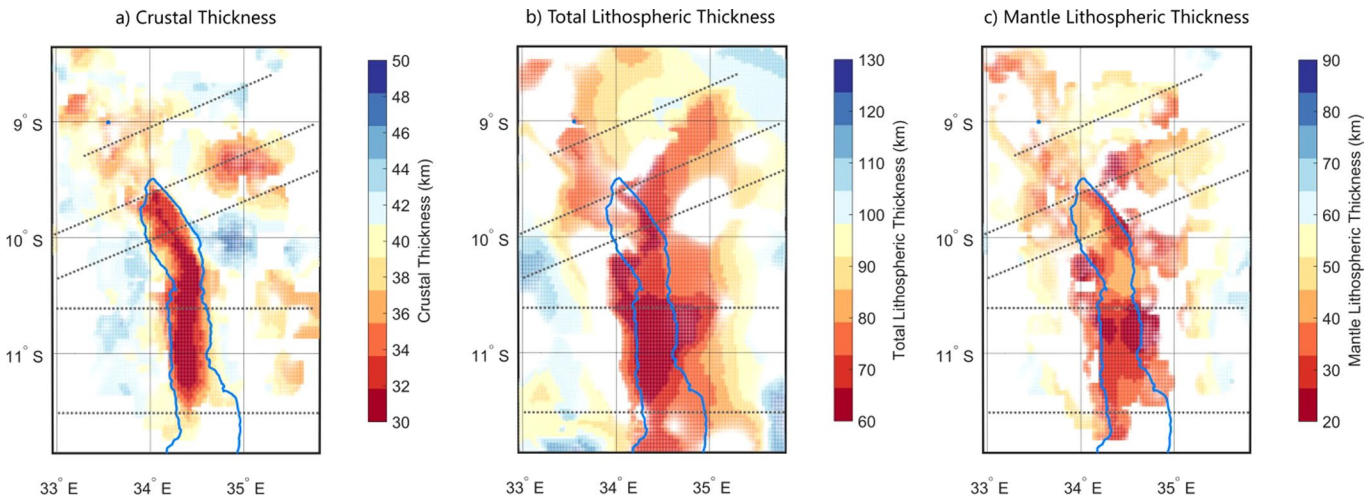
Reprints and permissions information is available at www.nature.com/reprints.

Content courtesy of Springer Nature, terms of use apply. Rights reserved



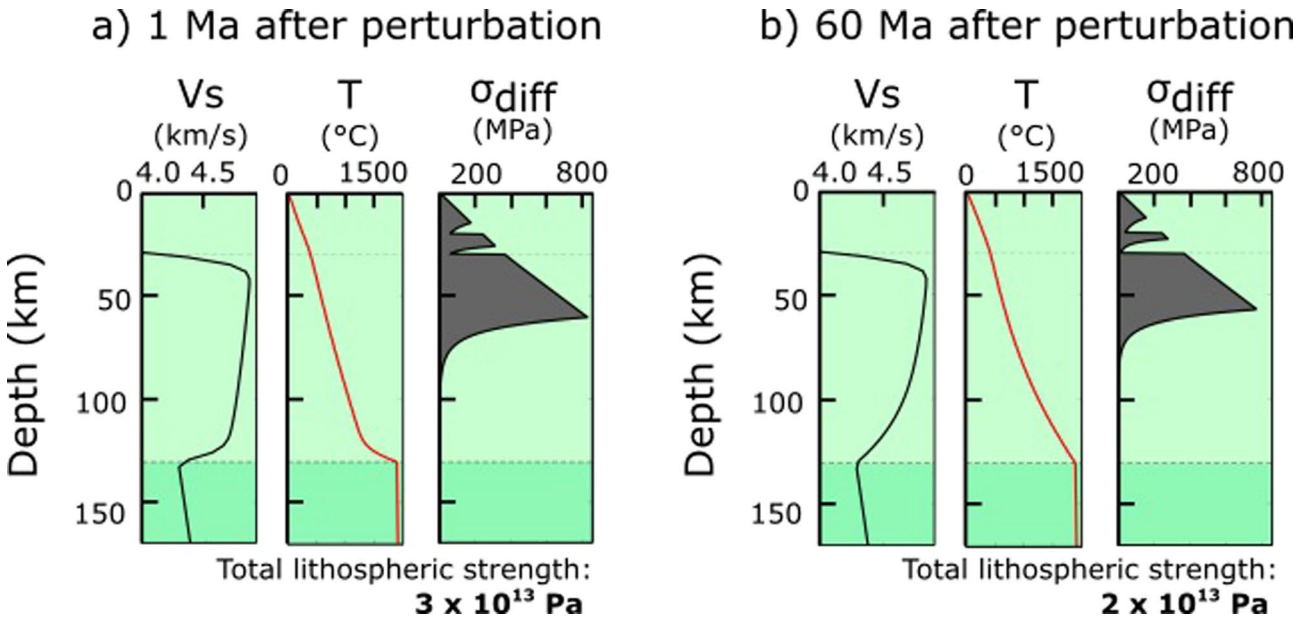
Extended Data Fig. 1 | Crustal structure beneath Lake Malawi. Cross sections are through the mean bootstrapped 1–100 s Ps common-conversion-point stack, masked by standard deviation between bootstraps (second colour bar) or fewer than 3 contributing waveforms (dark grey). 2x vertical exaggeration. Dashed black lines: Moho, picked from this Ps stack. Grey dashed lines: uncertainty on Moho (± 3 km). Black open symbols correspond to crustal estimates from other studies: circles[27]; diamonds[55]; triangle[53]; inverted triangle[29]. Where symbol is missing error bars, the reported uncertainty was smaller than the symbol. Red circles correspond to those on the location map (Fig. 1b). Shaded boxes correspond to terranes (Fig. 1a). Solid black line: topography at 10x v.e., blue across Lake Malawi.

Content courtesy of Springer Nature, terms of use apply. Rights reserved



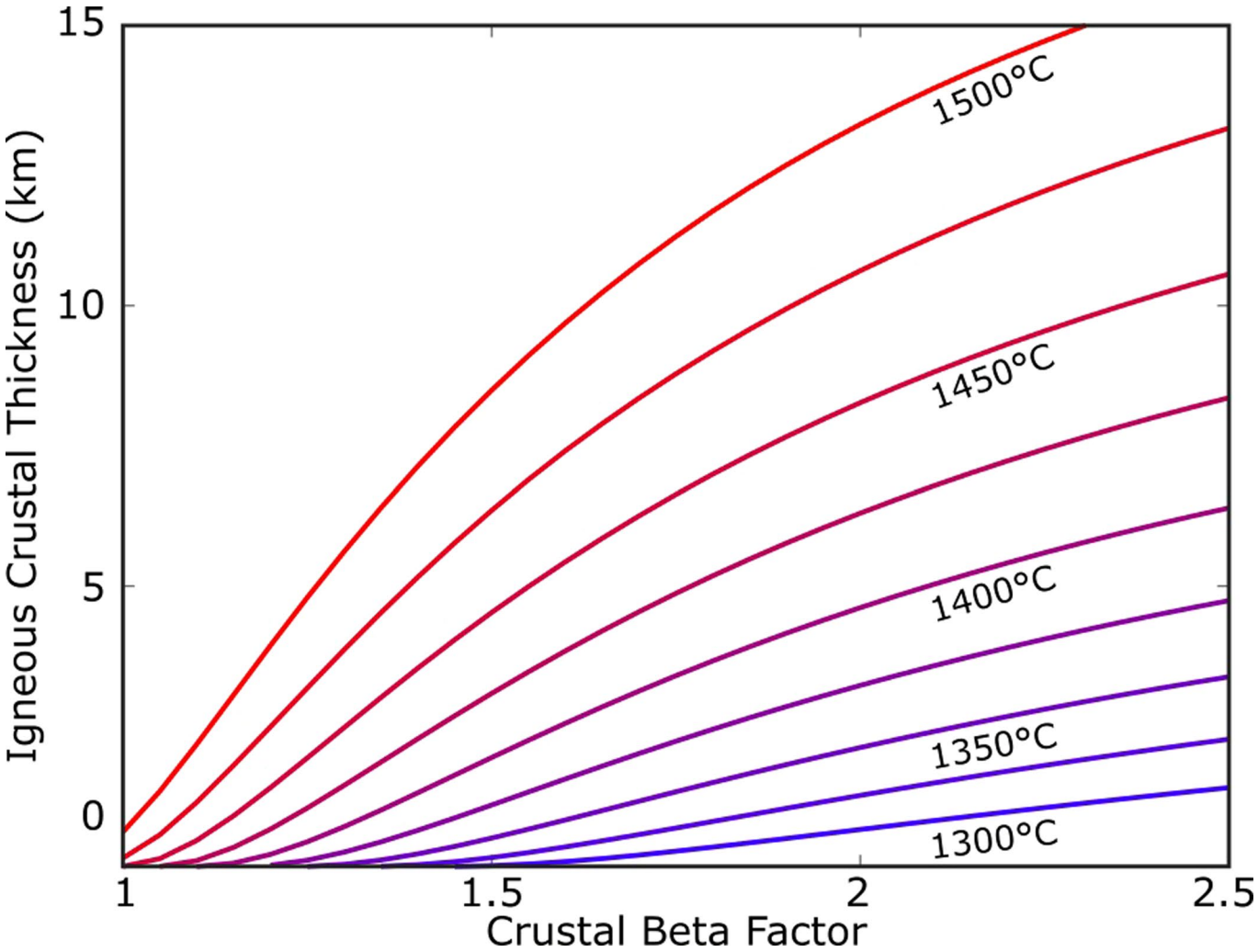
Extended Data Fig. 2 | Layer thicknesses used in calculating beta. Opacity scaled by standard deviation (as in Figs. 2, 3, S1). Plotted thicknesses are within 0.25° of a converted-wave pick, save crustal thickness beneath Lake Malawi. Grey lines: cross section locations (Fig. 2, S1). Blue line: Lake Malawi. **a**) Crustal thickness: difference between the topography (incorporating sedimentary basins in Lake Malawi[25]) and the Moho PVG. Crustal thickness beneath Lake Malawi is not masked as extrapolated crustal thicknesses are compatible with active source inversions[55]. **b**) Lithospheric thickness: difference between the topography and the LAB NVG. **c**) Lithospheric mantle thickness: difference between the Moho and the LAB. The mask is the maximum of the previous two panels.

Content courtesy of Springer Nature, terms of use apply. Rights reserved



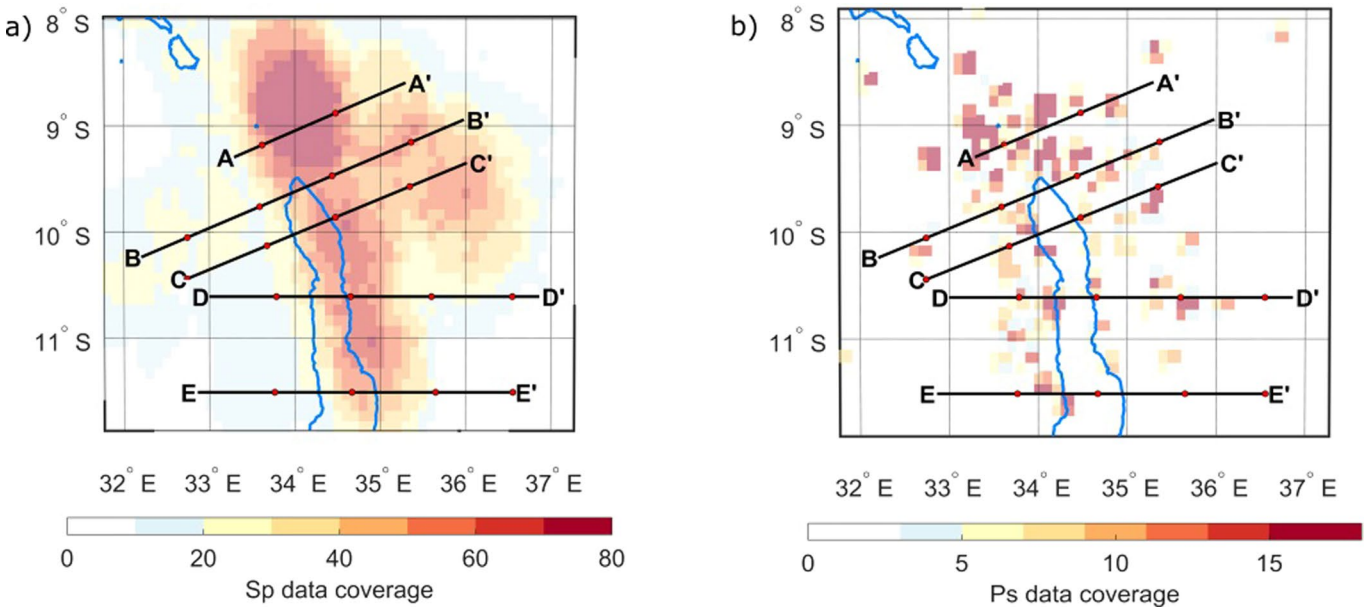
Extended Data Fig. 3 | Shear velocity, geotherm and yield strength envelope demonstrating the effect of conductive heating alone. a) Geotherm reflects conditions soon after a large (500 °C) asthenospheric temperature anomaly perturbs the previously equilibrated geotherm. **b**) Same panels after 60 Ma of thermal evolution. This timescale is longer than the total age of the East African Rift System. Despite the large temperature anomaly and long timescale allowed for conduction, the lithosphere does not substantially weaken due to conductive heating alone.

Content courtesy of Springer Nature, terms of use apply. Rights reserved



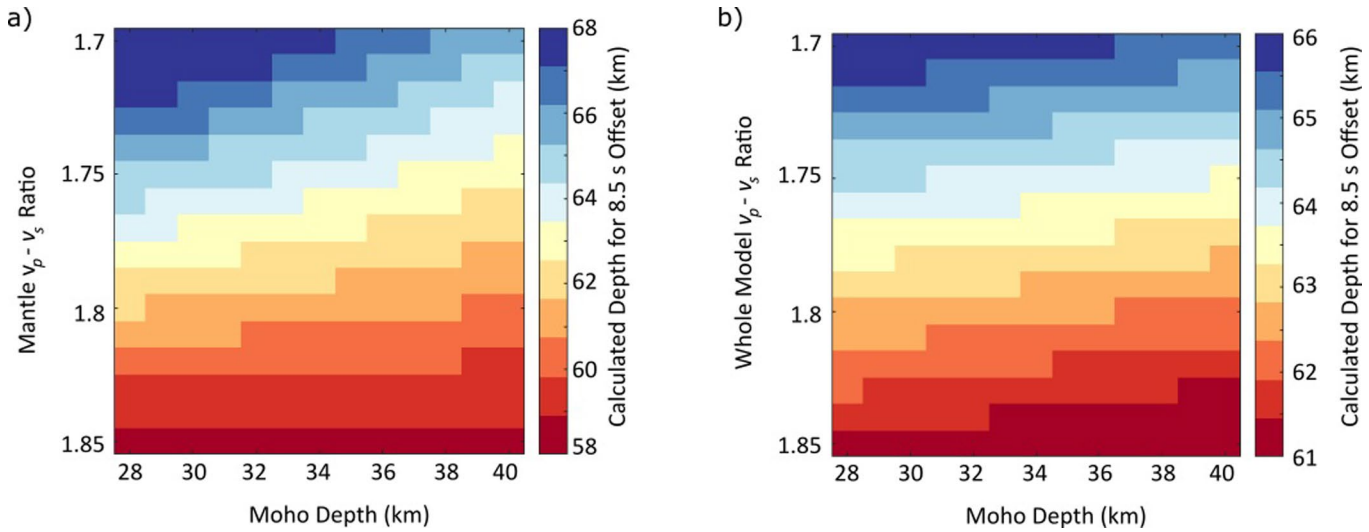
Extended Data Fig. 4 | Partial melt generated by lithospheric thinning. Integrated partial melt is displayed as total kilometres of igneous material added to the crust. Dependence on asthenospheric potential temperature and crustal beta factor are shown. In this calculation, lithospheric mantle thinning is assumed to be twice the magnitude of crustal thinning, based on our observations of present-day thinning across the Malawi Rift. Accardo et al. [14] estimate uppermost mantle temperatures most consistent with the cooler end of the range of potential temperatures shown here.

Content courtesy of Springer Nature, terms of use apply. Rights reserved



Extended Data Fig. 5 | Data coverage maps for common-conversion-point stacks. (**a**) Sp stack. (**b**) Ps stack. Solid black lines with red dots correspond to cross section locations (Figs. 2, S1). Blue line: Lake Malawi.

Content courtesy of Springer Nature, terms of use apply. Rights reserved



Extended Data Fig. 6 | Dependence of calculated LAB depth on migration model. LAB depths are calculated from the offset in seconds between the Sp and the primary S phases. The effect of Moho depth and v_P/v_S ratio are shown here across substantially larger ranges than the expected difference from the values used. These calculations are for a relatively short offset (8.5 s), relevant to the areas of thinnest lithosphere upon which our conceptual model is based. Given a longer observed offset, the changes due to v_P/v_S ratio will be slightly larger (e.g. for 16 s, varying v_P/v_S between 1.7-1.85 for a 34 km Moho is 116-129 km). (**a**) Depth variation assuming crustal v_P/v_S constrained by Borrego et al.[27] is correct, so v_P/v_S is varied only in the mantle. (**b**) Depth variation changing the v_P/v_S used across the whole depth range of the velocity model.

Content courtesy of Springer Nature, terms of use apply. Rights reserved

Terms and Conditions

Springer Nature journal content, brought to you courtesy of Springer Nature Customer Service Center GmbH (“Springer Nature”).
Springer Nature supports a reasonable amount of sharing of research papers by authors, subscribers and authorised users (“Users”), for small-scale personal, non-commercial use provided that all copyright, trade and service marks and other proprietary notices are maintained. By accessing, sharing, receiving or otherwise using the Springer Nature journal content you agree to these terms of use (“Terms”). For these purposes, Springer Nature considers academic use (by researchers and students) to be non-commercial.
These Terms are supplementary and will apply in addition to any applicable website terms and conditions, a relevant site licence or a personal subscription. These Terms will prevail over any conflict or ambiguity with regards to the relevant terms, a site licence or a personal subscription (to the extent of the conflict or ambiguity only). For Creative Commons-licensed articles, the terms of the Creative Commons license used will apply.
We collect and use personal data to provide access to the Springer Nature journal content. We may also use these personal data internally within ResearchGate and Springer Nature and as agreed share it, in an anonymised way, for purposes of tracking, analysis and reporting. We will not otherwise disclose your personal data outside the ResearchGate or the Springer Nature group of companies unless we have your permission as detailed in the Privacy Policy.
While Users may use the Springer Nature journal content for small scale, personal non-commercial use, it is important to note that Users may not:

1. use such content for the purpose of providing other users with access on a regular or large scale basis or as a means to circumvent access control;
2. use such content where to do so would be considered a criminal or statutory offence in any jurisdiction, or gives rise to civil liability, or is otherwise unlawful;
3. falsely or misleadingly imply or suggest endorsement, approval , sponsorship, or association unless explicitly agreed to by Springer Nature in writing;
4. use bots or other automated methods to access the content or redirect messages
5. override any security feature or exclusionary protocol; or
6. share the content in order to create substitute for Springer Nature products or services or a systematic database of Springer Nature journal content.

In line with the restriction against commercial use, Springer Nature does not permit the creation of a product or service that creates revenue, royalties, rent or income from our content or its inclusion as part of a paid for service or for other commercial gain. Springer Nature journal content cannot be used for inter-library loans and librarians may not upload Springer Nature journal content on a large scale into their, or any other, institutional repository.
These terms of use are reviewed regularly and may be amended at any time. Springer Nature is not obligated to publish any information or content on this website and may remove it or features or functionality at our sole discretion, at any time with or without notice. Springer Nature may revoke this licence to you at any time and remove access to any copies of the Springer Nature journal content which have been saved.
To the fullest extent permitted by law, Springer Nature makes no warranties, representations or guarantees to Users, either express or implied with respect to the Springer nature journal content and all parties disclaim and waive any implied warranties or warranties imposed by law, including merchantability or fitness for any particular purpose.
Please note that these rights do not automatically extend to content, data or other material published by Springer Nature that may be licensed from third parties.
If you would like to use or distribute our Springer Nature journal content to a wider audience or on a regular basis or in any other manner not expressly permitted by these Terms, please contact Springer Nature at

onlineservice@springernature.com